


Parameter-free quantitative simulation of high-dose microstructure and hydrogen retention in ion-irradiated tungsten

Daniel R. Mason ^{1,*} Fredric Granberg ² Max Boleininger,¹ Thomas Schwarz-Selinger ³ Kai Nordlund ² and Sergei L. Dudarev ¹

¹UK Atomic Energy Authority, Culham Science Centre, Oxfordshire OX14 3DB, United Kingdom

²Department of Physics, University of Helsinki, P.O. Box 43, FI-00014 Helsinki, Finland

³Max-Planck-Institut für Plasmaphysik, Boltzmannstrasse 2, 85748 Garching, Germany



(Received 24 June 2021; accepted 11 August 2021; published 17 September 2021)

Hydrogen isotopes are retained in plasma-facing fusion materials, triggering hydrogen embrittlement and changing tritium inventory as a function of exposure to neutron irradiation. But modeling highly damaged materials—exposed to over 0.1 displacements per atom (dpa)—where saturation of damage is often observed, is difficult because a microstructure containing high density of defects evolves nonlinearly as a function of dose. In this study we show how to determine the defect and hydrogen isotope content in tungsten exposed to high irradiation dose, using no adjustable or fitting parameters. First, we generate converged high dose (>1 dpa) microstructures, using a combination of the creation-relaxation algorithm and collision cascade simulations. Then we make robust estimates of vacancy and void regions using a modified Wigner-Seitz decomposition. The resulting estimates of the void surface area enable predicting the deuterium retention capacity of tungsten as a function of radiation exposure. The predictions are compared to ³He nuclear reaction analysis measurements of tungsten samples, self-irradiated at 290 K to different damage doses and exposed to low-energy deuterium plasma at 370 K. The theory gives an excellent match to the experimental data, with both model and experiment showing that 1.5–2.0 at.% deuterium is retained in irradiated tungsten in the limit of high dose.

DOI: [10.1103/PhysRevMaterials.5.095403](https://doi.org/10.1103/PhysRevMaterials.5.095403)

I. INTRODUCTION

Materials intended for the first wall and divertor of DEMO fusion reactor are expected to face irradiation doses of 10 dpa or more depending on location [1,2]. In the absence of comprehensive experimental data on materials that have actually experienced such high neutron fluxes with realistic fusion energy spectra, it is expected that device performance can be extrapolated to some extent using modeling and simulation. However, in recent years it has become increasingly clear that the methods developed to simulate microstructural evolution in the *dilute* defect limit are not well suited to generate representative *highly irradiated* microstructures. While it is correct to model an isolated prismatic dislocation loop as a diffusing single entity [3,4], and substantial progress has been made with object kinetic Monte Carlo [5–9] and cluster dynamics models [10,11], based on discrete defect objects with parameterized effective mobilities, this approach must break down in the limit where the defect concentration grows to the point when mean free paths are short or elastic interactions dominate the dynamics.

Correlated motion of defects is observed in theoretical models incorporating elastic interactions [12–14], which are able to explain the experimentally observed phenomena involving loop rafting [15,16] and self-pinning of defects [17]. In the dense microstructure limit often observed at doses

above ~ 0.1 dpa, new phenomena appear—dislocation loops can merge together to the point where they are better described as regions of near-perfect crystal than as isolated platelets of interstitial point defects [18,19]. This is a fundamental topological transition in irradiated materials between the point where dislocation objects can be treated as loops, to the point where dislocations form a material-spanning network [20]. Small changes in stress due to the production or movement of defects can unlock barriers previously too high to be overcome, leading to an avalanche of defect coalescence or recombination over a wide spatial extent [20]. Thermal activation controls the long time evolution of complex microstructures [21], but in the dense limit, their generation and description requires adequate handling of the large number of degrees of freedom involved in complex defect rearrangement [22–26].

The dense microstructure limit does have one simplifying universal feature, namely that the saturation of physical phenomena has been observed. Materials irradiated to >1 dpa at relatively low temperatures have shown saturation in thermal diffusivity [27], lattice strain [19], and hardness [28]. This suggests that, starting from some dose, further exposure to irradiation does not significantly evolve the defect distributions, and therefore we may have a chance to simulate this dynamic steady state even while the highly detailed modeling of nonlinear transient microstructural configurations remains difficult.

In this paper we interpret the experimental observations showing that the vacancy content of ion-irradiated tungsten,

*Daniel.Mason@ukaea.uk

as deduced using positron annihilation spectroscopy, exhibits saturation [29], as does its deuterium retention capacity [30–33] observed at relatively low temperatures and high dose (>0.2 dpa). We are able to explain experimental observations by simulating a dynamic steady state of a highly irradiated tungsten, characterized by fluctuating but statistically stationary vacancy distribution, which is modeled with atomic resolution using no adjustable or fitting parameters.

In a fusion reactor, it is necessary to keep a careful inventory of the tritium retained in the materials, both for the purpose of efficient tritium breeding and for minimizing its retention at the point of decommissioning or a loss-of-coolant accident [34,35]. Hydrogen mobility in crystalline tungsten is high, with an activation barrier of order 0.2 eV [36,37], and its enthalpy of solution is also high at order 1 eV [38,39]. Any hydrogen isotopes in crystalline tungsten will therefore either quickly migrate to existing defects [40], influencing their evolution [41,42], or even produce new defects [43–46].

Of the possible trapping sites for hydrogen in tungsten, a surface—either exterior or interior—is generally considered the most favorable location for hydrogen retention [39], with a binding energy of a hydrogen atom to the [100] surface of 0.7–0.9 eV [39], and to a vacancy 1.4 eV [47,48]. Up to six hydrogen atoms can be confined in a single vacancy at absolute zero. By contrast, the binding energy of a hydrogen atom to a self-interstitial atom defect is 0.3 eV [49], and to an interstitial dislocation loop 0.7 eV [50]. Hence, while hydrogen atoms can, in principle, form a Cottrell atmosphere in the elastic fields around dislocations, they are unlikely to be present in large concentrations around dislocations at room temperature except under constant plasma loading conditions [51].

Models for hydrogen retention typically start with the assumption of one or more defect trapping site types [52,53], and consider the effective diffusion of hydrogen from the traps to the surface or into the bulk [54]. Because of the difficulty associated with modifying these equations to take into account the nanoscale fluctuations in stresses observed in highly damaged microstructures [20], here we opt to find a theoretical maximum retention level based on the interior surface area of defects alone [55].

Previously, two simulation methodologies were employed to generate microstructures of heavily irradiated materials at the atomic scale.

The first method is the creation-relaxation algorithm (CRA) method [20], where instead of following full cascades, Frenkel pairs are directly inserted by removing randomly chosen atoms and replacing them in new, randomly chosen positions. The new configuration is then relaxed using conjugate gradients (CG) with appropriate elastic boundary conditions [18,20,56]. This is iterated many times to build up damage. As the canonical definition of displacements per atom (dpa) is the number of Frenkel pair production events generated by the algorithm per atom in a simulation cell [20], we have a well-defined measure of the (canonical) dpa level after any number of algorithmic steps. This canonical measure of dose is henceforth referred to as *cdpa*, to distinguish it from other measures of radiation exposure. The CRA method is very efficient in generating high dose microstructures. However, there is no temperature and no cascade effects, which have

been seen to be important in tungsten [57,58]. The number of defects obtained from a CRA simulation is therefore a theoretical maximum value, defined primarily by the buildup of internal fluctuating stress, and it is thought to overestimate the observed experimental effects [18,19].

The second method is to generate the radiation damage microstructures incrementally using a large number of overlapping sequential collision cascade simulations using molecular dynamics (MD). In a cascade simulation, one atom is given high kinetic energy, order kilovolts, or more, and the atomic system is then evolved in time with thermostats and barostats appropriate for the boundary conditions. This process is repeated as many times as can be afforded. This has been done for several metals, and doses achieved are on the order of tenths of a dpa [22,59–62]. The results of these simulations agree with Rutherford back scattering channeling measurements on similarly irradiated samples [63]. However, as one needs to cumulatively add up the dose, over 10 000 consecutive cascade simulations would be needed to reach one dpa. This limits the dose range that can be investigated using this direct cascade simulation approach.

To investigate converged heavily irradiated microstructures, without the need of tens of thousands of direct cascade simulations, we combine these two methods. We carry out cascade simulation to transform the CRA pregenerated microstructures to form atomic configurations with an effective dose up to several dpa. The convergence of this approach is demonstrated by extending computationally expensive cascade-only simulations to high dose. This convergence is found to be robust and significant, and it links together a purely static relaxation method for generating microstructure (CRA) with a dynamic time-dependent simulation method (MD), in a parameter-free way.

We emphasize that we do not claim the microstructures are thermally annealed. To our knowledge there does not exist any simulation technique yet for annealing a highly damaged microstructure, involving thousands of vacancies and dozens of arbitrarily complex interstitial loops and dislocation lines in a million-atom simulation cell, to experimental timescales.

To compute the void content, we need new methods of structural analysis of atomic configurations suited for highly irradiated systems. We discuss how to generate the optimal Wigner-Seitz (W-S) point defect counts using a strained and rotated reference crystal and show how to generate isosurfaces enclosing voids using this reference crystal. By this method we can separate vacancies in vacancy dislocation loops, a mismatch between the number of atoms and the number of reference lattice sites but with no empty space for a hydrogen atom, from vacancies isolated or in small clusters which act as strong trapping sites.

Finally, we use the computed void surface area to estimate hydrogen retention in highly damaged microstructures and discuss the relationship with experimental measurements.

II. METHODS

A. Simulations

To produce representative microstructures of tungsten, corresponding to high exposure to irradiation at doses up to 3 dpa,

we follow a two-step process—first using the CRA method [20] to generate the high-dose prerelaxed atomic structures, followed by further relaxation achieved by means of sequential overlapping MD cascade simulations.

As starting configurations, we use the CRA-generated atomic structures of tungsten explored in Ref. [19]. These structures were generated using the MNB interatomic tungsten potential, which is known to predict vacancy structures that agree well with DFT simulations [64]. The simulation cell contained 64×64 conventional cubic bcc unit cells in the x and y directions, and 200 unit cells in the z direction. The strain was set to zero in the x and y directions in the plane parallel to the surface of the sample, representing a constraint on the damaged layer due to the pristine defect-free extended substrate material below the surface layer of the material exposed to irradiation, and the homogeneous stress was kept at zero in the z direction, reflecting the traction-free surface boundary conditions. The simulations represent a section cut from a foil with a damaged top layer, such as might be produced by heavy ion bombardment. Maintaining zero stress in the z direction reflects the ability of the material to freely expand outwards in the direction normal to the surface, this enables modeling the effect of traction-free surface boundary conditions on the evolution of microstructure without explicitly including surfaces in the simulation. The simulations were performed using the molecular dynamics simulation package LAMMPS [65].

As very large local stresses are generated by the build up of point defects, a single CRA step can produce major atomistic rearrangement over a large spatial extent [20]. As dose increases, dislocation loops are formed, as interstitials are inherently mobile under stress. At a dose of order 0.1 cdpa, the dislocation loops combine into a dislocation network, changing the apparent number of atomic lattice planes in the simulation cell. Vacancies are relatively immobile in a CRA simulation, hence voids do not form. Importantly, as the only mode of relaxation of atomic structures is essentially downhill in energy, the CRA method does not easily overcome potential barriers. The microstructures produced by CRA simulations are typically very dense in defects [19].

A computational approach similar to the massively overlapping cascade simulations [22,59–61] was used in our investigation to achieve full microstructural convergence in the limit of high dose. The simulations were carried out with the MD code PARCAS [66,67], with an adaptive timestep to account for the movement of high energy atoms [68]. Electronic stopping was applied as a friction force acting on all the atoms with a kinetic energy over 10 eV [69]. The interatomic potential was the same as that used in the CRA simulations [64].

A perfect bcc simulation cell was created with the size $64 \times 64 \times 200$ conventional cubic bcc unit cells, containing about 1 600 000 atoms. The cell was created with the lattice constant corresponding to the temperature of 300 K. The simulation cell was then thermalized to 300 K with fixed cell dimensions in the two shorter directions and kept at zero stress in the longest dimension. After the initial relaxation and thermalization, consecutive atomic impacts were initiated in the cell as follows. (i) A 10-keV cascade was initialized in the center of the cell, with a Berendsen thermostat [70] at the

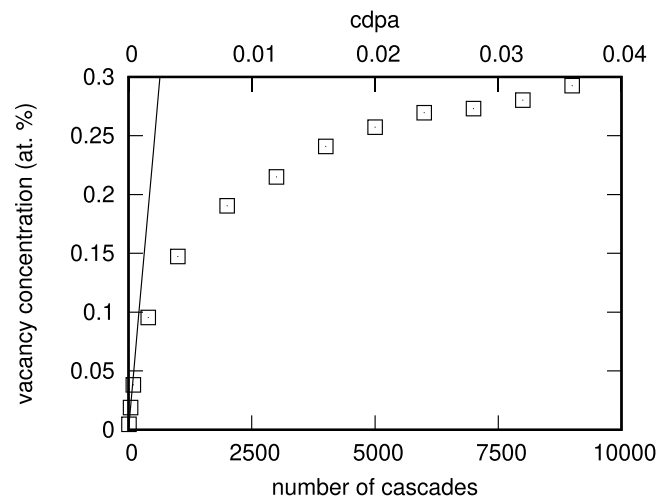


FIG. 1. Vacancy concentration as a function of MD cascade count. The canonical dpa rate is the gradient of vacancy concentration as a function of N_{casc} at $N_{\text{casc}} = 0$, indicated by the solid line.

border atoms and no pressure control. This was simulated for 20 ps. (ii) The cell was then relaxed with thermostat on all atoms and a pressure control [70] to keep zero pressure in the longest dimension, this simulation lasted for 10 ps. (iii) After the relaxation, the cell was shifted randomly over the periodic boundaries, in order for the next cascade to occur in a different region, to obtain a homogeneous irradiation of the entire cell. (iv) This was repeated many times. Two independent runs were conducted to assess possible statistical differences; it was concluded that the differences were small.

As the canonical definition of displacements per atom is related to the number of vacancies generated in a perfect crystal in the limit of zero dose, the cdpa rate for the sequential cascade events is given by the rate of increase of vacancy concentration per lattice site c_v , with the number of cascades N_{casc}

$$\text{cdpa} = \left. \frac{\partial c_v}{\partial N_{\text{casc}}} \right|_{N_{\text{casc}}=0} N_{\text{casc}}. \quad (1)$$

In Fig. 1 we plot the vacancy content using the W-S method for our MD-only cascade simulations. Using the data derived from the first 40 cascade simulations, we find that $\text{cdpa} = 4.07 \times 10^{-6} N_{\text{casc}}$.

We observe that the volume vacancy fraction reaches a concentration close to 0.3 at.%. This agrees with experimental observations on ion-irradiated tungsten [27] and other metals [71], as well as simulations performed on other metals [22,59,60]. We extended these MD cascade simulations out to 10 000 cascades, equivalent to 0.04 cdpa over a total simulation time interval of 300 ns.

Simulations of microstructural relaxation driven by cascades followed the same procedure as described above. The starting point for cascade simulations were the highly damaged cells generated by CRA simulations [20] using the cell geometry defined in Ref. [19]. As starting configurations for cascade simulations, we took the CRA configurations corresponding to the damage doses of 0.0063, 0.019, 0.035, 0.063, 0.11, 0.19, 0.35, 0.63, 1.1, and 3.0 cdpa. These cells were

initially scaled to the correct lattice constant (at 300 K) and thermalized to room temperature over 10 ps using a Berendsen thermostat [70], with the same boundary conditions as described above. After the initial thermalization, 1600 PKAs of 10 keV each were initiated in the cell. This corresponds to an extra exposure of 0.0065 cdpa in each case.

B. Defect detection

In this subsection we develop methods for detecting point defects and defect clusters in high-dose atomistic simulations. This methodological development is necessary as lattice defects are defined by deviations from a reference lattice, but at high dose the concept of a reference atomic lattice can become ill-defined; the average distorted lattice certainly can no longer be assumed to be same as the initial zero-dose perfect lattice configuration. Furthermore, in what follows we choose to compare the results of our simulations to deuterium retention experiments, which we will argue are a good measure of the vacancy content, and so is a good proxy measure of the correctness of our generated microstructure. We therefore need to distinguish between unoccupied lattice sites, typically defined in the context of the Wigner-Seitz analysis—which could, for example, be part of a vacancy dislocation loop and hence associated with relatively minor tensile strain while exhibiting no substantial local free volume sufficient for accommodating a deuterium atom—from true “voids,” which we can define simply as being well-localized excess empty spaces between the atoms.

The Wigner-Seitz method is commonly used to identify the positions of point defects in crystalline materials in the low-damage limit [67]. This technique imagines the Voronoi tessellation of an ideal lattice. Atoms are placed into these Voronoi volumes, and the number of atoms in each Voronoi volume is counted separately. If the atom positions are close to the reference lattice sites, each volume is taken as being singly occupied. If the atoms are significantly displaced from reference ideal lattice sites, then some volumes will have zero occupancy, others multiple occupancy. The volumes with zero occupancy are then marked as vacancies, even if the actual amount of free volume in a “vacancy” defined in this way is very small. In practice, the Voronoi geometry does not need to be calculated, it suffices to find the nearest reference site to each atom.

We are, in principle, free to choose our reference lattice. In the dilute defect case, corresponding to the low dose, this is rarely a problem—we use the original perfect lattice defined by the asymptotic positions of sites far from the defect(s). In the dense defect case we still need to formulate a rule that would determine what to take as a reference. Consider the simulation supercell to be a periodically repeating parallelepiped with repeat vectors $\vec{A}_1, \vec{A}_2, \vec{A}_3$. By definition, for each point \vec{x} there is an equivalent point $\vec{x} + N_1\vec{A}_1 + N_2\vec{A}_2 + N_3\vec{A}_3$, where N_α are integers ($\alpha = \{1, 2, 3\}$).

Now consider a reference lattice of *primitive* unit cells. This again is a periodically repeating parallelepiped with repeat vectors $\vec{b}_1, \vec{b}_2, \vec{b}_3$. By definition, for each point \vec{z} there is an equivalent point $\vec{z} + n_1\vec{b}_1 + n_2\vec{b}_2 + n_3\vec{b}_3$, where n_α are integers.

For the two cells to be commensurate, it is necessary only for any triplet $\{N_1, N_2, N_3\}$ for there to exist a triplet $\{n_1, n_2, n_3\}$, such that

$$N_1\vec{A}_1 + N_2\vec{A}_2 + N_3\vec{A}_3 = n_1\vec{b}_1 + n_2\vec{b}_2 + n_3\vec{b}_3. \quad (2)$$

Given the linearity of the problem, this reduces to

$$\vec{A}_\alpha = n_{1\alpha}\vec{b}_1 + n_{2\alpha}\vec{b}_2 + n_{3\alpha}\vec{b}_3, \quad (3)$$

or, in matrix notation $\mathbf{A} = \mathbf{b} \cdot \mathbf{n}$, where $A_{\beta\alpha}$ is the β th Cartesian component of the α th vector. The matrix \mathbf{n} is a matrix of nine independent integers, which has the flexibility to consider any combination of axial strains, shears, and rotations necessary to fit the primitive unit cell into the simulation supercell.

Given the simulation cell \mathbf{A} , and an intention to use, say, a bcc primitive cell with $\vec{b}_1 = a_0[\bar{1}11]$ and so on, a fit for the number of unit cell repeats is

$$\mathbf{n} = \text{nint}[\mathbf{b}^{-1}\mathbf{A}], \quad (4)$$

where $\text{nint}[\mathbf{b}^{-1}\mathbf{A}]$ is the component-wise nearest-integer operator. The best fit unit cell, strained and rotated appropriately, is then

$$\tilde{\mathbf{b}} = \mathbf{A}\mathbf{n}^{-1}. \quad (5)$$

Note that there is no requirement for \mathbf{n} to remain constant through a simulation, particularly one with high-dose damage where new crystal planes could be formed. The counts of interstitials and vacant sites are not constrained to be equal.

We may have an estimate for the homogeneous rotation and strain in the atomic system. This could be done by analyzing the position of the peaks of the square of the structure factor $S(\vec{q}) = \sum_i \exp[i\vec{q} \cdot \vec{x}_i]$, where the sum runs over all atom positions \vec{x}_i . Then we have a better starting estimate for the primitive cell $\mathbf{T}^0\mathbf{b}$, and we can use this in place of \mathbf{b} in Eq. (4). We describe how we find a homogeneous transformation matrix \mathbf{T}^0 using a real-space method in the Appendix.

The primitive unit cell has an associated motif \vec{y}_i , $i = \{1, 2, \dots\}$ associated with it. For the bcc and fcc cases there is only one motif point, but hcp and diamond structure have two. The lattice is invariant under translation of the motif. In the dense defect case, where displacements may be large, there can arise a disregistry between the reference lattice and the displaced planes of atoms. This will typically manifest as smooth planar regions of point defects. We can therefore say that the optimal translation for the Wigner-Seitz reference is the one with *fewest point defects*. This is a global minimization problem, hard to solve generally, as an arbitrarily small displacement may push an atom from matching one reference site to another. We find a good lattice offset with a simple grid search; we search $6 \times 6 \times 6$ trial offsets on a uniform grid, establish the one with the fewest point defects, then refine the grid and search again. This process is repeated a third time, giving a reasonably high-precision estimate for a minimum.

Finally, we note that this procedure will still fail if there are multiple grains or phases in the system. We used common neighbor analysis [72,73] to search for subgrains in our simulation boxes, but did not find any. Therefore we leave the multigrain defect detection problem for future research.

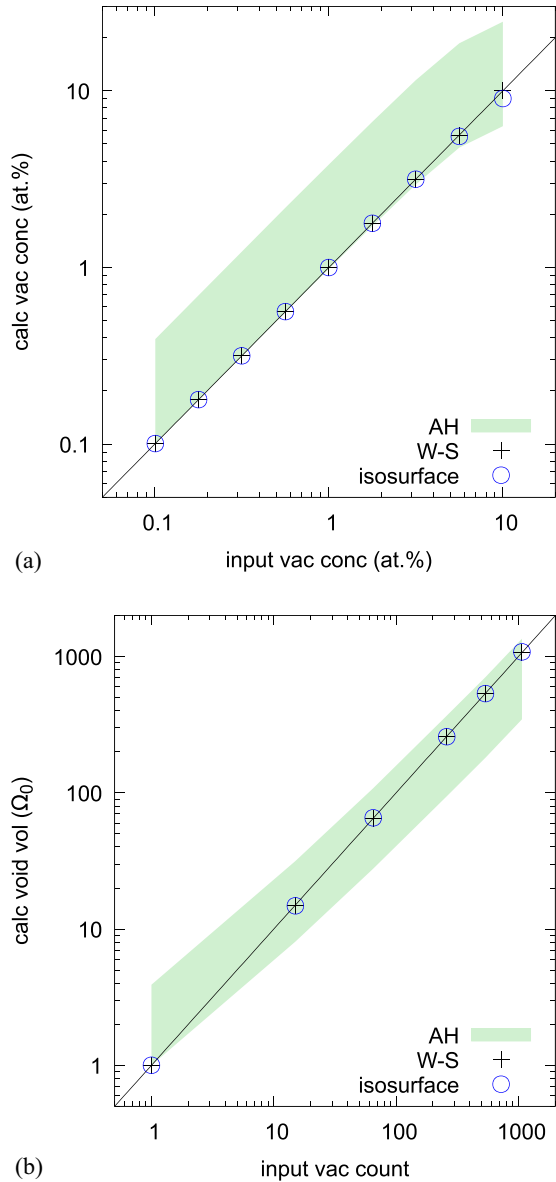


FIG. 2. A comparison of three vacancy detection methods: alpha hull (AH), Wigner-Seitz (W-S), and the isosurface method developed here. (a) Performance of defect detection algorithms with homogeneously distributed vacancies. (b) Performance with single spherical void. Solid line indicates perfect vacancy counting. Note the W-S algorithm performs perfectly in these cases.

The successful operation of the W-S method to determine unoccupied lattice sites is illustrated in Fig. 2.

An alternate choice for detecting void spaces between the atoms, which are large enough for storing deuterium, is to construct the alpha-hull (AH) from the Delaunay tetrahedralization of the atomic positions.

This method requires a single input parameter, a minimum sphere radius used to determine concave surfaces, and so is highly transferable across atomic structures. It is a robust method for determining the number and location of voids within a body, and is implemented in OVITO as the construct surface mesh modifier [74]. It does, however, produce surfaces with nodes defined by atomic positions. The volume

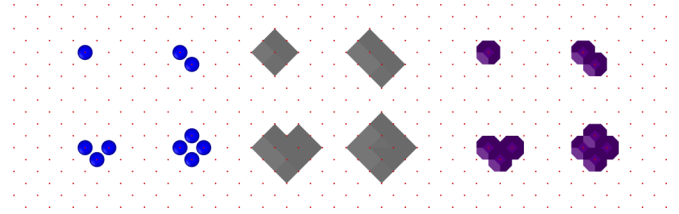


FIG. 3. Small vacancy clusters identified using Wigner-Seitz occupation (left), Delaunay triangulation (AH method) (center), and Wigner-Seitz isosurfaces, described here (right).

of a monovacancy region is, therefore, overestimated, and the surface produced does not have the symmetry of the Wigner-Seitz cell. The void-bounding surfaces produced for small vacancy clusters are illustrated in Fig. 3. Note that for this bcc example, the void surface for a monovacancy is dodecahedral, and encloses a volume $4\Omega_0$. Volumes and surface areas of larger vacancy cluster regions can also be reported, but with no simple linear transformation to determine the number of point defects represented. In Fig. 2 we illustrate this issue by representing the vacancy count using the AH method as a band. The lower limit assumes that one vacancy has volume $4\Omega_0$, and is correct for homogeneous distributions. The upper limit assumes one vacancy has volume Ω_0 , and is asymptotically correct for large voids.

Now we describe a new method that sits between the W-S and AH approaches. If we know the lattice type, we can define vectors to the *expected* positions of neighbors. Writing \vec{x}_i as the position of atom i , and $\vec{v}_{k,i}$ as the vector from i to the expected location of neighbor k , the k th Wigner-Seitz plane passes through the midpoint of \vec{x}_i and $\vec{x}_i + \vec{v}_{k,i}$, and so is defined by the plane

$$\left(\frac{2\vec{v}_{k,i}}{|\vec{v}_{k,i}|^2}\right) \cdot (\vec{x} - \vec{x}_i) = 1. \quad (6)$$

Defining the k th normal vector as $\vec{n}_{k,i} = 2\vec{v}_{k,i}/|\vec{v}_{k,i}|^2$, we can find a scalar field $\psi_i(\vec{x})$ defining the distance from atom i preserving the symmetry of the Wigner-Seitz cell

$$\psi_i(\vec{x}) = \max_k \{|\vec{n}_{k,i} \cdot (\vec{x} - \vec{x}_i)|\}. \quad (7)$$

The region closest to atom i in the perfect lattice satisfies $\psi_i(\vec{x}) < 1$. We can then define a scalar field $\phi(\vec{x})$ describing distance from any atomic position as the minimum value of $\psi_i(\vec{x})$

$$\phi(\vec{x}) = \min_i \{\psi_i(\vec{x})\}. \quad (8)$$

In an ideal lattice, this will have the value zero at atomic positions, rising to 1 at the Wigner-Seitz cell boundary. If there is a void, then $\phi(\vec{x}) > 1$ in this region. We illustrate a $\phi = 1$ isosurface bounding small vacancy clusters in Fig. 3. For the bcc lattice we see that the isosurface is a truncated octahedron, which is the correct shape for the Wigner-Seitz cell.

If the lattice is not ideal, but instead is characterized by a local strain tensor and rotation, then the vectors to neighbors can be found from those in the reference lattice $\{\vec{v}_{k,i}^0\}$ by

$$\vec{v}_{k,i} = \mathbf{T}(\vec{x}_i)\vec{v}_{k,i}^0, \quad (9)$$

where $\mathbf{T} = (\mathbf{I} + \epsilon)\mathbf{R}$ is a combined rotation and strain at point \bar{x}_i . We describe how to compute a converged local strain field $\mathbf{T}(\bar{x})$ in the Appendix.

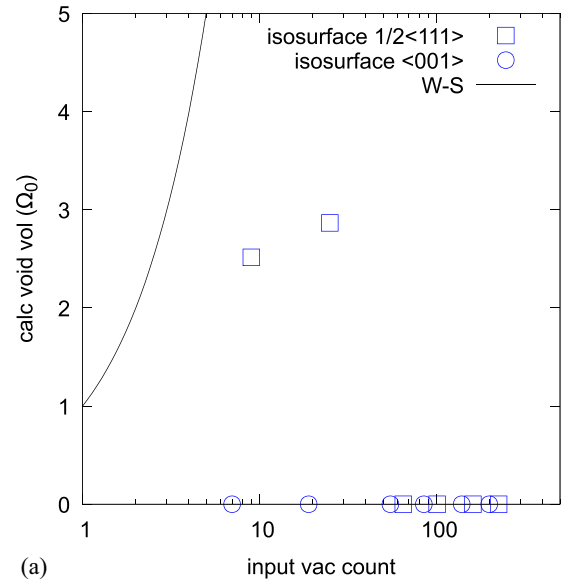
To compute the isosurface at $\phi = 1$ in practice, we note that thermal fluctuations might make small “cracks” appear at isosurface level $\phi = 1$ simply because atoms, in a fluctuating manner, might be instantaneously further away from each other than expected. To compensate for this, we can compute the volume and area at isosurface level $\phi = 1 + \epsilon$, where ϵ is a small parameter of the order of the (fractional) vibration lengthscale of the atoms. This effectively redraws the Wigner-Seitz planes slightly further distant from the atoms, shrinking the void regions proportionately. We therefore also compute the volume and area derivatives of the isosurface with respect to ϵ , and extrapolate to find the volume and area at exactly $\phi = 1$. Volume and area are not sensitive to the choice of ϵ , we find taking $\epsilon = 0.05$ works well in all cases we tested. The correct performance of our isosurface algorithm for simple homogeneous vacancies and voids is demonstrated in Fig. 2, where we show the calculated vacancy concentration for given input vacancy concentrations for W-S, AH, and our isosurface method.

In Fig. 4 we demonstrate where our algorithm differs from W-S. For prismatic vacancy loops with Burgers vectors $\vec{b} = 1/2\langle 111 \rangle$, we find no void space, whereas W-S finds a difference between the number of lattice points and the number of atoms. For prismatic vacancy loops with $\vec{b} = \langle 001 \rangle$, relaxed using the MNB potential [64], we find small voids opening at the dislocation core. This core shows a remarkable connection with the work by Bullough [75] who noted that the core of an edge dislocation with a large Burgers vector can be treated analogously to a crack.

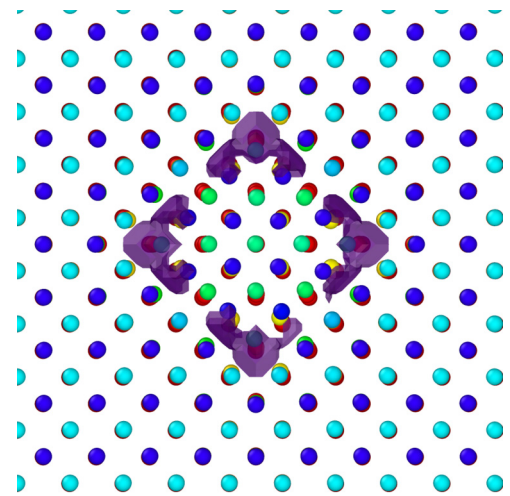
Figure 5 illustrates one of our CRA + MD simulation cells at 1 cdpa, analyzed using the defect detection algorithms described here. We can see a one-to-one match between the voids detected using our isosurfaces method and monovacancies/small vacancy clusters detected with the Wigner-Seitz method, except for at the vacancy dislocation loops. These are readily identified as planar features of higher “point defect” density in the central cell circled by dislocation lines. Note that some isosurfaces cross the periodic boundaries and appear as flecks. The bottom replica shows a slice through the local strain calculation, generated to improve the local estimation of the Wigner-Seitz normal vectors.

C. Experimental methods

Tungsten samples with nominal 99.97 at.% purity were procured from Plansee [76], outgassed, and annealed at 2000 K for 3 minutes, producing large grains with 10–50 μm diameter and a low dislocation density estimated at $2 \times 10^{10} \text{ m}^{-2}$ [77]. The samples were irradiated to different damage dose ranging from 0.001 to 2.3 dpa at the damage peak maximum using 20.3 MeV W^{6+} self ions at room temperature at the TOF beamline of the 3-MV tandetron accelerator at the Max-Planck-Institut für Plasmaphysik. Details can be found in Ref. [78]. Damage doses were estimated using the Fast Kinchin-Pease option using SRIM [79,80], with a threshold displacement energy of 90 eV [81].



(a)



(b)

FIG. 4. A comparison of the Wigner-Seitz (W-S) algorithm to the isosurface method developed here when applied to vacancy loops. (a) Performance of void detection algorithm with prismatic vacancy loops in bcc tungsten. Two Burgers vectors ($\mathbf{b} = 1/2\langle 111 \rangle \dots$ and $\mathbf{b} = \langle 001 \rangle$) are considered. Note that the W-S algorithm returns the number of vacant lattice sites exactly, whereas the isosurface method usually returns zero void space. (b) Slice through a $[001]$ vacancy loop viewed in the $[001]$ orientation containing 25 vacant lattice sites, atoms colored by depth. Isosurface showing the position of four voids overlaid.

The samples were then exposed simultaneously to a low-temperature deuterium (D) plasma to decorate the produced defects with a moderate ion flux of $5.6 \times 10^{19} \text{ D m}^{-2}\text{s}^{-1}$. For the chosen plasma parameters this ion flux hitting the samples contains dominantly D_3^+ ions with an energy below 15 eV. The target holder temperature was set with a liquid-cooled thermostat to 370 K, which is adequate to allow D diffusion into the bulk, and hence into the traps associated with radiation defects, but does not cause evolution of the traps themselves [82]. For these exposure conditions the D retention

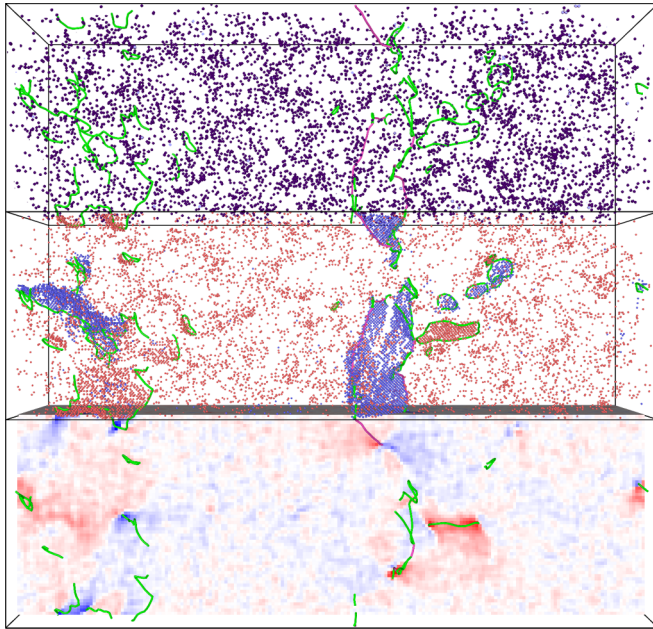


FIG. 5. A simulation cell generated with CRA simulations to 1 cdpa, then relaxed with MD cascades. The periodic replicas show (top) void detection using isosurfaces; (center) Wigner-Seitz point defect detection shows vacancies (red) and interstitials (blue); (bottom) local strain calculation showing the ϵ_{xz} component colored from blue (compressive -5%) through white (no strain) to red (tensile $+5\%$), where z is the long axis direction (here shown horizontally). A dxa analysis [73] is overlaid to show the dislocation loops and network. Green lines have Burgers vector $1/2\langle 111 \rangle$ and pink lines $\langle 100 \rangle$. Visualisation performed with OVITO [74].

is trap-limited, rather than diffusion limited, and the solute D atoms are not in equilibrium with the trapped population. A full description of this implantation methodology can be found in Refs. [78,83].

The retained deuterium population was analysed *ex situ* using the $D(^3\text{He},p)\alpha$ nuclear reaction, with eight different ^3He energies ranging from 500 to 4500 keV chosen to probe the sample depth up to $7.4 \mu\text{m}$. A full description of the NRA analysis methodology used is given in Ref. [42].

III. RESULTS AND DISCUSSION

The results of application of the combined CRA + MD cascade microstructure simulations are shown in Fig. 6. The clearly visible convergence of combined CRA and MD cascade simulations shown in this figure is the main finding of this work. In the figure, the solid line corresponds to the massively overlapping cascade simulations alone, and the squares to the CRA + MD cascade microstructure simulation results. The CRA + MD cascade simulations are shown at these increments: before any cascade and after 10, 25, 50, 100, 200, 400, 600, 800, 1000, 1200, 1400, and 1600 cascades. Note that these increments are not linear.

In Fig. 6, each different color set starts with a CRA only simulation—i.e., zero number of MD cascades. This point corresponds to the highest vacancy concentration in the microstructure. Subsequent points on the cascade relaxation

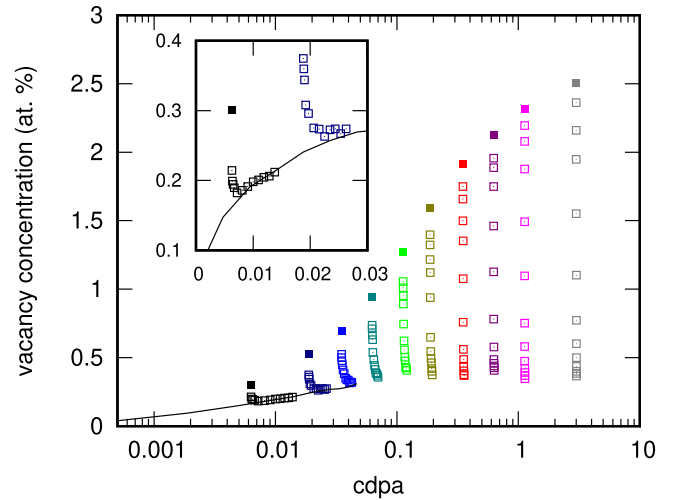


FIG. 6. CRA simulations annealed with MD cascades. Solid symbols: CRA simulation only. Open symbols: CRA simulations with MD annealing. Solid line: MD cascades only, i.e., perfect lattice starting point. Inset: Same data plotted on a linear scale shows a match between MD cascade only and CRA + MD simulation techniques.

curve show the effect of MD cascades on the microstructure. The vacancy concentration initially shows a dramatic reduction after just a few MD cascades, then the convergence rate gradually decreases until a converged limit is found.

First, looking at the three lowest starting points, corresponding to the lowest doses in the CRA method, we can clearly see the cascade relaxation effect, which reduces the fraction of vacancies in the microstructure. This reduction continues until the solid line (MD-only simulations) is reached. We observe that as the number of cascades increases past this point, so does the vacancy fraction, in excellent agreement with the solid line. This validates that the combined method is resulting in the same defect concentration as the massively overlapping cascade simulations alone, however, here already with a speed up of a factor of 2 to 5 depending on the CRA starting point.

Second, looking at the high dose starting points, we again can observe a huge effect of cascade relaxation in the beginning, with a small effect at the end of the run. We see a saturation of vacancy concentration at a level of 0.3 at.%. This is an order of magnitude drop in vacancy concentration compared to the CRA-only simulations. With the direct validation against massively overlapping cascades at the lower doses and with the qualitative agreement (both defect concentration level and overall behavior), we observe this combined technique to be very effective on obtaining microstructures at very high doses—the microstructures obtained by combining CRA + MD can result in a dose which would otherwise require about 1 million overlapping cascade simulations. This represents a dramatic computational speed-up on the order of 500.

The resulting counts of all the point defect types determined for our high-dose simulations is shown in Fig. 7. We find the interstitial count, and the total count of unoccupied lattice sites using the W-S method. The proportion

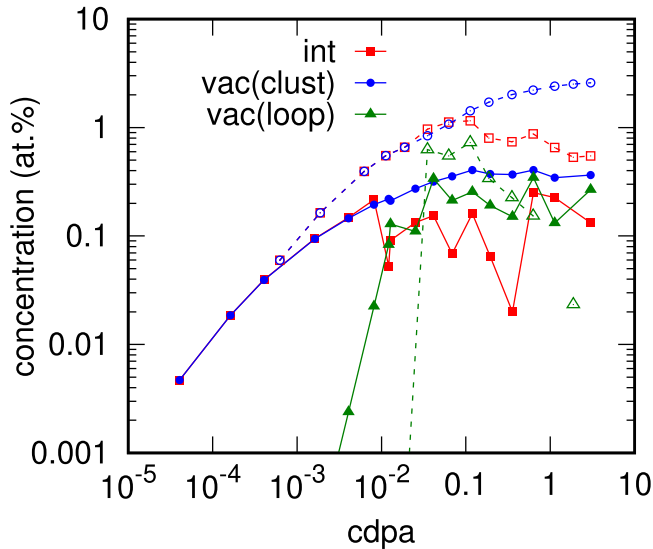


FIG. 7. A count of point defects for high dose microstructure simulations. Interstitials counted using W-S method. Vacancies in clusters counted using isosurface method, and vacancies in loops taken as difference between total vacant lattice sites (W-S) and vacancies in clusters. Open symbols are the result of using CRA simulations alone. Solid symbols are the result of using MD and CRA + MD relaxed simulations. The lines are to guide the eye between sets of points.

of vacancies in vacancy loops is found by subtracting the vacancies counted using the isosurface method from the total Wigner-Seitz count of unoccupied lattice sites. In this plot we use an extended range of CRA-only simulations to emphasize the regime where interstitial and vacancy counts are equal. We see that the atomic fraction of vacancies increases linearly with dose at low fluence, but tends to saturate at high fluence, with CRA at 2.5 at.% and CRA + MD at 0.3 at.%. This order of magnitude difference is clearly very significant for predicting properties of highly irradiated materials, and demonstrates the importance of further relaxation of CRA-simulated microstructures. The interstitial count is seen to follow the vacancy count at low fluence—this is an expected consequence of defects being generated as Frenkel pairs. But at high fluence, interstitial dislocation loops extend across the periodic boundaries of the cell and form complete planes of atoms, with residual network dislocations. For example, in the simulation snapshot in Fig. 5, the matrix of primitive cell repeats is

$$\mathbf{n} = \begin{pmatrix} 0 & 64 & 201 \\ 64 & 0 & 201 \\ 64 & 64 & 1 \end{pmatrix}, \quad (10)$$

indicating that, compared to the original zero dose simulation box, an additional plane normal to the z direction with Burgers vector $1/2\langle 111 \rangle$ has formed.

It is notable that this split between interstitial and vacancy count occurs earlier in the simulations with cascades, at 0.01 dpa compared to 0.1 dpa in the CRA-only simulations. This occurs because the high-energy cascade MD simulations provide sufficient energy for the defect clusters to overcome thermal barriers. We also see that vacancy loops emerge nat-

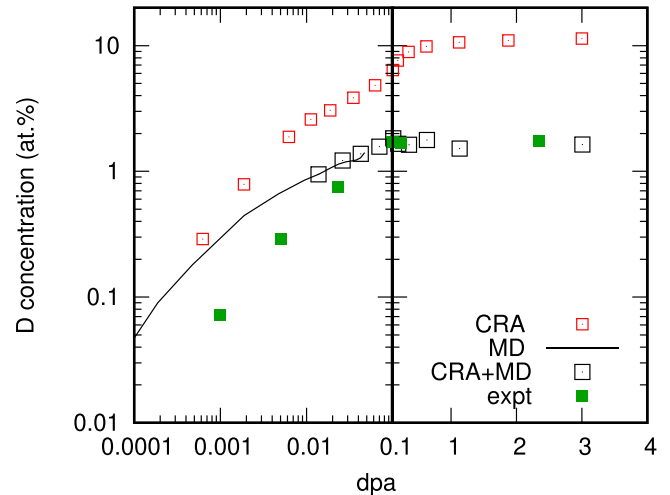


FIG. 8. Deuterium (D) concentration assuming 5 D atoms per monovacancy equivalent. Note the displacement damage scale x -axis is split into logarithmic and linear halves to emphasize the saturation level in the high dose limit.

urally in both CRA and CRA + MD simulations, and with a similar atomic fraction, at the point where interstitial and vacancy counts diverge. They can be clearly seen in Fig. 5. These vacancy loops are generated by *interstitial* loop coalescence: indeed, when the interstitial dislocation loops coalesce to form a full new atomic lattice plane they will not do so with 100% coverage, but rather will leave small gaps, like holes in the complete atomic planes. These gaps remain bounded by edge dislocation lines. They are, by definition therefore, vacancy loops.

To make an estimate for the amount of hydrogen that can be retained in the material from the defect concentrations computed above, we need to estimate the trapping efficiency of the defects in our simulated microstructure. This has been studied in detail in Ref. [84] for the 0.23 dpa data point shown in Fig. 8. There the authors simulated the experimental results using a macroscopic rate equation code [85], assuming three defect types [86] with trapping energies corresponding to monovacancies and vacancy clusters. As this modeling gives a good fit to the experimental data, without recourse to hydrogen trapping on other defects, we will also assume here that it is the vacancies which are most significant in relation to hydrogen retention.

Our approach will differ by how we determine the count of trapped deuterium (D) atoms per vacancy. Previously, a great deal of work has gone into evaluating the trapping energies for individual deuterium traps [87], and this information is invaluable for modeling outgassing as a function of temperature, such as in thermal desorption spectroscopy. Here our goal is only to determine the maximum amount of retained deuterium. We instead use a model inspired by Hayward and Fu [55,88]. They showed, using density functional calculations, that hydrogen saturates the surface of vacancy clusters in α -Fe before forming H_2 gas bubbles within, so that the important relevant parameter is the void surface area. In tungsten this is likely also to be so, as in our simulations the vacancy clusters do not grow significantly. Given that the monova-

cancy is generally considered to trap up to five hydrogen atoms at room temperature [86], and that these occupy five of the six $[1/200]$ interstitial positions surrounding the vacant site, we can use the simple model that the surface area of a monovacancy is 5/6 occupied.

If we generalize this result and consider the internal surface area of void spaces to be the relevant factor in determining the deuterium retention capacity, we need make no distinction here between monovacancies, vacancy clusters or voids, or indeed the more difficult to characterize internal surfaces such as seen in Fig. 4. A more sophisticated model might make a distinction with a gas bubble containing D_2 in the empty volume, but as we have little vacancy aggregation in our low-temperature simulations or experiments we leave this to future work. For a general vacancy cluster with surface area Σ , computed using the isosurface method above, we say that the number of deuterium atoms retained, n_D , is

$$n_D = 5 \frac{\Sigma}{\Sigma_V}, \quad (11)$$

where Σ_V is the surface area of a monovacancy.

Figure 8 shows the final outcome of our analysis, an estimation of the maximum deuterium concentration possible in irradiated simulation cells, compared with direct NRA measurements of the concentration of D in irradiated tungsten. We see that the CRA-only simulations greatly overestimate the saturation level, suggesting a D concentration over 10 at.%. This is understood as a consequence of the overestimation of vacancy-type defects in CRA simulations due to the incomplete relaxation of the microstructure. The combined CRA + MD simulations, however, offer an excellent estimation of the D retention, at order 1.5–2.0 at.% in the saturation limit. The most significant difference between the experimentally measured D concentration and our simulated estimate is the offsetting of the damage scale (x -axis). This is not unexpected in this case, as the simulations use a canonical measure of the number of vacancies produced by the simulation, whereas the experiment uses a measure defined by counting the number of Frenkel pairs created in binary collisions, assuming a somewhat uncertain threshold energy for this process. The experiment also can allow some additional long-time thermal relaxation of defects at room temperature which cannot presently be accounted for in the detailed exploration of defect microstructures.

IV. CONCLUSION

In this study, we demonstrated how to generate converged microstructures of a material exposed to high radiation dose, using a combination of the creation-relaxation algorithm and molecular dynamics cascade simulations.

As the CRA method depends on static relaxations, displaced atoms can only be moved to a nearby local minimum energy configuration. By contrast, MD can overcome thermal activation barriers, and so can move between local minima. Even a small amount of MD will therefore relax high-energy configurations to some extent. Cascade simulations introduce sufficient energy to overcome much higher barriers than an equivalent time of thermal annealing alone, and so act as simulated annealing on high dose CRA configurations. This

simulated annealing removes the “memory” of the initial condition, replacing high-energy CRA microstructure with lower energy MD microstructure. In this paper we showed that the computational time required for this process is reasonable, and by matching the definition of canonical displacements per atom we also match almost perfectly the defect content of CRA + MD simulations with MD cascade simulations alone.

We showed that the Wigner-Seitz methodology for finding defects can be employed to interpret the highly dense defect microstructures. We discussed how to generate the correct reference lattice, even when the simulation cell is sheared or rotated, using a technique based on simple matrix inversion. We refined this reference lattice by taking into account the measurable homogeneous deformation, and adjusting the offset of the lattice motif. We further showed that this standard measure of the occupation of lattice sites gives a good estimator of the point defect numbers, but if we want to discriminate between vacancies appearing as voids and those appearing in vacancy loops we can do this by finding isosurfaces in the Wigner-Seitz occupation. By this means we were able to compute not just the number of vacant reference lattice sites, but rather the surface area of voids in the simulation.

In our simulations, relaxation is performed by MD cascades rather than by “true” thermal annealing, and so there is still little vacancy mobility, and little void growth. This is probably a reasonable assumption to compare to experiments performed at temperatures below the onset of vacancy mobility, as we have done here, but our methodology for generating microstructures will need to be supplemented by thermal annealing to compare to higher temperature experimental results.

There are few divacancies, and the surface area of a divacancy is just slightly under the surface area of two monovacancies. Therefore the fractional surface area measured is, in this case, a close match to the fraction of vacant lattice sites. Importantly, we demonstrated a defect detection methodology which continues to work accurately even when voids do form under irradiation.

In this study we did not consider the external surface area of the target itself as a trapping site for deuterium. The quality of a highly irradiated surface can vary considerably due to the effects of sputtering and deposition [45,89,90]. Our experimental study used NRA, which is a depth resolved method (for characteristic depth traces the reader is referred to Refs. [78,91]). One can deduce from these measurements that for our reported experimental procedure, deuterium retention at the external surface is of minor importance. Our simulations used periodic boundary conditions and so have no explicit surface. Our results therefore compare, in experiment and simulation, the *internal* surfaces that can be drawn around monovacancies, vacancy clusters, and voids. We found that the internal surface area increases linearly with dose for low dose, but then flattens and saturates between 0.01 and 0.1 dpa. Using a simple model for hydrogen retention, based on 5/6 of the possible vacancy cluster surface area being occupied, we find a very good match to the concentration of retained hydrogen implanted from a plasma into irradiated tungsten.

As our model for hydrogen retention is essentially parameter-free, depending solely on a robust estimation of the total vacancy surface area, we would expect it to be able to

reproduce the changes in hydrogen retention due to changes in microstructure observed by changing the elastic boundary conditions, or by introducing impurity atom types.

ACKNOWLEDGMENTS

This work has been carried out within the framework of the EUROfusion Consortium and has received funding from the Euratom research and training program 2014-2018 and 2019-2020 under Grant No. 633053 and from the RCUK (Grant No. EP/T012250/1). To obtain further information on the data and models underlying this paper please contact PublicationsManager@ukaea.uk. The views and opinions expressed herein do not necessarily reflect those of the European Commission. We would like to thank P.-W. Ma and F. Hofmann for stimulating discussions. Computer time granted by the IT Center for Science (CSC) Finland is gratefully acknowledged.

APPENDIX: COMPUTING LOCAL DEFORMATION GRADIENT

In this section we will describe the algorithm used to compute the local rotation and strain fields. This is done with an iterative real-space method. If we know the lattice type, then from atom i at position \bar{x}_i , we would expect to find its k th neighbor at position $(\bar{x}_i + \bar{v}_{k,i}^0)_{\min}$ if the lattice were locally perfect [92]. In the perfect crystal, each atom in the same sublattice is expected to have neighbors at the same vector positions. If we actually find that atom i has a neighbor at a position $\bar{x}_i + \bar{v}_{k,i}$, where $\bar{v}_{k,i}$ is not the expected ideal lattice vector, then we can use this information to find the local strain. This is a simple task where strains are small, but around a dislocation core this may not be true and care must be taken.

The basis of the strain-finding algorithm is to minimize a fitting function of the form

$$S_i = \sum_k (\mathbf{T}\bar{v}_{k,i}^0 + \bar{\delta} - \bar{v}_{k,i})^2, \quad (\text{A1})$$

with respect to the nine matrix elements of the matrix \mathbf{T} and the three elements of a uniform vector offset $\bar{\delta}$. Differentiating Eq. (A1) with respect to these 12 elements gives a set of simultaneous linear equations, which can be solved with the Lapack routine DSYSV. In our code we use a simple link-cell list [93] to find the neighbors of atom i . This returns an unsorted list of neighbor vectors $\bar{v}_{j,i}$. We sort this list by pairing each member of $\bar{v}_{j,i}$ with the expected vector $\bar{v}_{k,i}^0$ which has the smallest separation $|\bar{v}_{j,i} - \bar{v}_{k,i}^0|$, rejecting any vector for which $|\bar{v}_{j,i} - \bar{v}_{k,i}^0| > a_0/4$ for all k , where a_0 is the lattice parameter. With the list sorted we can minimize the fit function, but we could still find unexpected results if we applied Eq. (A1) unthinkingly atom-by-atom, as our matching is making an implicit assumption that the strain is small.

To ensure a reasonably smoothly varying local strain, we note that we can add weighting and an initial guess to

Eq. (A1). Let us imagine we minimized $\sum_i S_i$ and found a global homogeneous strain \mathbf{T}^0 and offset $\bar{\delta}^0$ which best matches all the atoms simultaneously. We can now write $\bar{v}_{k,i}^1 = \mathbf{T}^0 \bar{v}_{k,i}^0 + \bar{\delta}^0$, and pair the observed set of neighbors to this new set of expected positions. Then we can optimize

$$S = \sum_i w_i \sum_k (\mathbf{T}\bar{v}_{k,i}^1 + \bar{\delta} - \bar{v}_{k,i})^2, \quad (\text{A2})$$

where now $\bar{v}_{k,i}$ is a neighbor to atom i paired with expected neighbor vector $\bar{v}_{k,i}^1$, and w_i is a weighting for atom i . This is the same set of simultaneous equations, but now each expected neighbor position is strained, rotated, and shifted.

We can make a locally varying estimate of the strain by setting the weights w_i with a Gaussian function centered on a point \bar{x} and width σ .

$$w_i = \text{Exp}\left[-\frac{|\bar{x}_i - \bar{x}|^2}{2\sigma^2}\right]. \quad (\text{A3})$$

Now minimizing Eq. (A2) finds the best strain locally to \bar{x} . If $\sigma = \infty$, then each atom is weighted equally, and Eq. (A2) returns a slightly improved solution to the homogeneous strain given by the matrix product $\mathbf{T}\mathbf{T}^0$, and offset $\mathbf{T}\bar{\delta}^0 + \bar{\delta}$. If our initial guess was good, we expect \mathbf{T} to be close to the identity and $|\bar{\delta}|$ small.

To refine the local strains, we compute Eq. (A2) on an evenly spaced mesh of nodes spanning the supercell with spacing σ set to the shortest supercell dimension, and \bar{x} placed on each node in turn, taking the homogeneous solution $\bar{v}_{k,i}^1$ as our initial guess. This gives a new set of spatially varying strains $\mathbf{T}^1(\bar{x}) = \mathbf{T}(\bar{x})\mathbf{T}^0$, and displacements $\bar{\delta}^1(\bar{x}) = \mathbf{T}(\bar{x})\bar{\delta}^0 + \bar{\delta}(\bar{x})$ on the nodes. Importantly, because we chose σ to be large, this makes $\mathbf{T}(\bar{x})$ near unity and slowly varying.

We then make a linear interpolation of strains and displacements to a new mesh of nodes with spacing $\sigma/4$, to seed a new spatially refined estimate of the expected atom positions, $\bar{v}_{k,i}^2(\bar{x}) = \mathbf{T}^1(\bar{x})\bar{v}_{k,i}^1 + \bar{\delta}^1(\bar{x})$. This process is iterated, each time reducing the mesh spacing, computing a small local change in the strain and displacement, and the small local change in the expected positions of the neighbors. By this process we can build up a potentially large local transformation from small incremental steps. We stop the iteration at the n th level when $\sigma \approx a_0$, and we have an evenly spaced mesh of nodes with the spacing of the lattice parameter.

Note that the derivative of the local displacement vector $\bar{\delta}^n$ produced at the end of the iteration is not related to the local strain—these displacements are only used to match observed neighbours to expected neighbors and improve the fit for the strain. We discard it.

The final local rotostrain transformation $\mathbf{T}(\bar{x})$ at a general point \bar{x} used in Eq. (9) is needed as a continuous field, so is taken to be the linear interpolation of the final iteration $\mathbf{T}^n(\bar{x})$ computed on the eight nodes nearest to \bar{x} .

[1] J. H. You, E. Visca, C. Bachmann, T. Barrett, F. Crescenzi, M. Fursdon, H. Greuner, D. Guilhem, P. Languille, M. Li, S. McIntosh, A. V. Müller, J. Reiser, M. Richou, and M.

Rieth, European DEMO divertor target: Operational requirements and material-design interface, *Nucl. Mater. Energy* **9**, 171 (2016).

- [2] M. R. Gilbert, S. Zheng, R. Kemp, L. W. Packer, S. L. Dudarev, and J.-Ch. Sublet, Comparative assessment of material performance in DEMO fusion reactors, *Fusion Sci. Technol.* **66**, 9 (2014).
- [3] P. M. Derlet, M. R. Gilbert, and S. L. Dudarev, Simulating dislocation loop internal dynamics and collective diffusion using stochastic differential equations, *Phys. Rev. B* **84**, 134109 (2011).
- [4] K. Arakawa, K. Ono, M. Isshiki, K. Mimura, M. Uchikoshi, and H. Mori, Observation of the one-dimensional diffusion of nanometer-sized dislocation loops, *Science* **318**, 956 (2007).
- [5] I. Martin-Bragado, A. Rivera, G. Valles, J. Luis Gomez-Selles, and M. J. Caturla, MMonCa: An object kinetic Monte Carlo simulator for damage irradiation evolution and defect diffusion, *Comput. Phys. Commun.* **184**, 2703 (2013).
- [6] C. Domain, C. S. Becquart, and L. Malerba, Simulation of radiation damage in Fe alloys: An object kinetic Monte Carlo approach, *J. Nucl. Mater.* **335**, 121 (2004).
- [7] R. E. Stoller, S. I. Golubov, C. Domain, and C. S. Becquart, Mean field rate theory and object kinetic Monte Carlo: A comparison of kinetic models, *J. Nucl. Mater.* **382**, 77 (2008).
- [8] C. S. Becquart and C. Domain, An object kinetic Monte Carlo simulation of the dynamics of helium and point defects in tungsten, *J. Nucl. Mater.* **385**, 223 (2009).
- [9] N. Castin, A. Dubinko, G. Bonny, A. Bakaev, J. Likonen, A. De Backer, A. E. Sand, K. Heinola, and D. Terentyev, The influence of carbon impurities on the formation of loops in tungsten irradiated with self-ions, *J. Nucl. Mater.* **527**, 151808 (2019).
- [10] J. Marian and V. V. Bulatov, Stochastic cluster dynamics method for simulations of multispecies irradiation damage accumulation, *J. Nucl. Mater.* **415**, 84 (2011).
- [11] C. Liu, L. He, Y. Zhai, B. Tyburska-Püschel, P. M. Voyles, K. Sridharan, D. Morgan, and I. Szlufarska, Evolution of small defect clusters in ion-irradiated 3C-SiC: Combined cluster dynamics modeling and experimental study, *Acta Mater.* **125**, 377 (2017).
- [12] S. L. Dudarev, M. R. Gilbert, K. Arakawa, H. Mori, Z. Yao, M. L. Jenkins, and P. M. Derlet, Langevin model for real-time Brownian dynamics of interacting nanodefects in irradiated metals, *Phys. Rev. B* **81**, 224107 (2010).
- [13] S. L. Dudarev, K. Arakawa, X. Yi, Z. Yao, M. L. Jenkins, M. R. Gilbert, and P. M. Derlet, Spatial ordering of nano-dislocation loops in ion-irradiated materials, *J. Nucl. Mater.* **455**, 16 (2014).
- [14] Y. Li, M. Boleininger, C. Robertson, L. Dupuy, and S. L. Dudarev, Diffusion and interaction of prismatic dislocation loops simulated by stochastic discrete dislocation dynamics, *Phys. Rev. Materials* **3**, 073805 (2019).
- [15] X. Yi, M. L. Jenkins, M. A. Kirk, Z. Zhou, and S. G. Roberts, In-situ TEM studies of 150 keV W⁺ ion irradiated W and W-alloys: Damage production and microstructural evolution, *Acta Mater.* **112**, 105 (2016).
- [16] O. El-Atwani, E. Aydogan, E. Esquivel, M. Efe, Y. Q. Wang, and S. A. Maloy, Detailed transmission electron microscopy study on the mechanism of dislocation loop rafting in tungsten, *Acta Mater.* **147**, 277 (2018).
- [17] D. R. Mason, X. Yi, M. A. Kirk, and S. L. Dudarev, Elastic trapping of dislocation loops in cascades in ion-irradiated tungsten foils, *J. Phys.: Condens. Matter* **26**, 375701 (2014).
- [18] A. Debelle, J.-P. Crocombette, A. Boulle, A. Chartier, T. Jourdan, S. Pellegrino, D. Bachiller-Perea, D. Carpentier, J. Channagiri, T.-Hien Nguyen, F. Garrido, and L. Thomé, Lattice strain in irradiated materials unveils a prevalent defect evolution mechanism, *Phys. Rev. Materials* **2**, 013604 (2018).
- [19] D. R. Mason, S. Das, P. M. Derlet, S. L. Dudarev, A. J. London, H. Yu, N. W. Phillips, D. Yang, K. Mizohata, R. Xu, and F. Hofmann, Observation of Transient and Asymptotic Driven Structural States of Tungsten Exposed to Radiation, *Phys. Rev. Lett.* **125**, 225503 (2020).
- [20] P. M. Derlet and S. L. Dudarev, Microscopic structure of a heavily irradiated material, *Phys. Rev. Materials* **4**, 023605 (2020).
- [21] F. Ferroni, X. Yi, K. Arakawa, S. P. Fitzgerald, P. D. Edmondson, and S. G. Roberts, High temperature annealing of ion irradiated tungsten, *Acta Mater.* **90**, 380 (2015).
- [22] F. Granberg, J. Byggmästar, and K. Nordlund, Defect accumulation and evolution during prolonged irradiation of Fe and FeCr alloys, *J. Nucl. Mater.* **528**, 151843 (2020).
- [23] A. E. Sand, J. Byggmästar, A. Zitting, and K. Nordlund, Defect structures and statistics in overlapping cascade damage in fusion-relevant bcc metals, *J. Nucl. Mater.* **511**, 64 (2018).
- [24] M.-C. Marinica, F. Willaime, and N. Mousseau, Energy landscape of small clusters of self-interstitial dumbbells in iron, *Phys. Rev. B* **83**, 094119 (2011).
- [25] D. R. Mason, A. E. Sand, and S. L. Dudarev, Atomistic-object kinetic Monte Carlo simulations of irradiation damage in tungsten, *Modell. Simul. Mater. Sci. Eng.* **27**, 055003 (2019).
- [26] T. D. Swinburne and D. Perez, Self-optimized construction of transition rate matrices from accelerated atomistic simulations with Bayesian uncertainty quantification, *Phys. Rev. Materials* **2**, 053802 (2018).
- [27] A. Reza, H. Yu, K. Mizohata, and F. Hofmann, Thermal diffusivity degradation and point defect density in self-ion implanted tungsten, *Acta Mater.* **193**, 270 (2020).
- [28] E. Gaganidze, C. Petersen, E. Materna-Morris, C. Dethloff, O. J. Weiß, J. Aktaa, A. Povstyanko, A. Fedoseev, O. Makarov, and V. Prokhorov, Mechanical properties and TEM examination of RAFM steels irradiated up to 70dpa in BOR-60, *J. Nucl. Mater.* **417**, 93 (2011).
- [29] A. Hollingsworth, M. Yu. Lavrentiev, R. Watkins, A. C. Davies, S. Davies, R. Smith, D. R. Mason, A. Baron-Wiechec, Z. Kollo, J. Hess, I. Jepu, J. Likonen, K. Heinola, K. Mizohata, E. Meslin, M.-F. Barthe, A. Widdowson, I. S. Grech, K. Abraham, E. Pender *et al.*, Comparative study of deuterium retention in irradiated eurofer and Fe-Cr from a new ion implantation materials facility, *Nucl. Fusion* **60**, 016024 (2019).
- [30] B. Tyburska, V. Kh. Alimov, O. V. Ogorodnikova, K. Schmid, and K. Ertl, Deuterium retention in self-damaged tungsten, *J. Nucl. Mater.* **395**, 150 (2009).
- [31] V. Kh. Alimov, Y. Hatano, B. Tyburska-Püschel, K. Sugiyama, I. Takagi, Y. Furuta, J. Dorner, M. Fusseder, K. Isobe, T. Yamanishi, and M. Matsuyama, Deuterium retention in tungsten damaged with W ions to various damage levels, *J. Nucl. Mater.* **441**, 280 (2013).
- [32] O. V. Ogorodnikova and V. Gann, Simulation of neutron-induced damage in tungsten by irradiation with energetic self-ions, *J. Nucl. Mater.* **460**, 60 (2015).
- [33] J. Wang, Y. Hatano, T. Hinoki, V. Kh. Alimov, A. V. Spitsyn, N. P. Bobyr, S. Kondo, T. Toyama, H. Tae Lee, Y. Ueda, and T. Schwarz-Selinger, Deuterium retention in W and binary W

- alloys irradiated with high energy Fe ions, *J. Nucl. Mater.* **545**, 152749 (2021).
- [34] R. A. Causey, Hydrogen isotope retention and recycling in fusion reactor plasma-facing components, *J. Nucl. Mater.* **300**, 91 (2002).
- [35] G. R. Tynan, R. P. Doerner, J. Barton, R. Chen, S. Cui, M. Simmonds, Y. Wang, J. S. Weaver, N. Mara, and S. Pathak, Deuterium retention and thermal conductivity in ion-beam displacement-damaged tungsten, *Nucl. Mater. Energy* **12**, 164 (2017).
- [36] K. Heinola and T. Ahlgren, Diffusion of hydrogen in bcc tungsten studied with first principle calculations, *J. Appl. Phys.* **107**, 113531 (2010).
- [37] G. Holzner, T. Schwarz-Selinger, T. Dürbeck, and U. von Toussaint, Solute diffusion of hydrogen isotopes in tungsten—a gas loading experiment, *Phys. Scr.*, **T171**, 014034 (2020).
- [38] R. Frauenfelder, Solution and diffusion of hydrogen in tungsten, *J. Vac. Sci. Technol.* **6**, 388 (1969).
- [39] K. Heinola and T. Ahlgren, First-principles study of H on the reconstructed W(100) surface, *Phys. Rev. B* **81**, 073409 (2010).
- [40] G.-H. Lu, H.-B. Zhou, and C. S. Becquart, A review of modelling and simulation of hydrogen behaviour in tungsten at different scales, *Nucl. Fusion* **54**, 086001 (2014).
- [41] D. Kato, H. Iwakiri, Y. Watanabe, K. Morishita, and T. Muroga, Super-saturated hydrogen effects on radiation damages in tungsten under the high-flux divertor plasma irradiation, *Nucl. Fusion* **55**, 083019 (2015).
- [42] T. Schwarz-Selinger, J. Bauer, S. Elgeti, and S. Markelj, Influence of the presence of deuterium on displacement damage in tungsten, *Nucl. Mater. Energy* **17**, 228 (2018).
- [43] Y.-N. Liu, T. Ahlgren, L. Bukonte, K. Nordlund, X. Shu, Y. Yu, X.-C. Li, and G.-H. Lu, Mechanism of vacancy formation induced by hydrogen in tungsten, *AIP Adv.*, **3** 122111 (2013).
- [44] S.-Y. Qin, S. Jin, L. Sun, H.-B. Zhou, Y. Zhang, and G.-H. Lu, Hydrogen assisted vacancy formation in tungsten: A first-principles investigation, *J. Nucl. Mater.* **465**, 135 (2015).
- [45] Y. Zayachuk, M. H. J. 't Hoen, P.A. Zeijlmans van Emmichoven, D. Terentyev, I. Uytendhouwen, and G. van Oost, Surface modification of tungsten and tungsten–tantalum alloys exposed to high-flux deuterium plasma and its impact on deuterium retention, *Nucl. Fusion* **53**, 013013 (2013).
- [46] E. A. Hodille, N. Fernandez, Z. A. Piazza, M. Ajmalghan, and Y. Ferro, Hydrogen supersaturated layers in H/D plasma-loaded tungsten: A global model based on thermodynamics, kinetics and density functional theory data, *Phys. Rev. Materials* **2**, 093802 (2018).
- [47] D. Kato, H. Iwakiri, and K. Morishita, First-principle study on binding energy of vacancy-hydrogen cluster in tungsten, *J. Soc. Plasma Sci. Nucl. Fusion Research Ser.* **8**, 404 (2009).
- [48] K. Heinola, T. Ahlgren, K. Nordlund, and J. Keinonen, Hydrogen interaction with point defects in tungsten, *Phys. Rev. B* **82**, 094102 (2010).
- [49] C. S. Becquart, C. Domain, U. Sarkar, A. De Backer, and M. Hou, Microstructural evolution of irradiated tungsten: *Ab initio* parameterisation of an OKMC model, *J. Nucl. Mater.* **403**, 75 (2010).
- [50] A. De Backer, D. R. Mason, C. Domain, D. Nguyen-Manh, M.-C. Marinica, L. Ventelon, C. S. Becquart, and S. L. Dudarev, Multiscale modelling of the interaction of hydrogen with interstitial defects and dislocations in BCC tungsten, *Nucl. Fusion* **58**, 016006 (2017).
- [51] A. De Backer, D. R. Mason, C. Domain, D. Nguyen-Manh, M.-C. Marinica, L. Ventelon, C. S. Becquart, and S. L. Dudarev, Hydrogen accumulation around dislocation loops and edge dislocations: from atomistic to mesoscopic scales in BCC tungsten, *Phys. Scr.*, **T170**, 014073 (2017).
- [52] M. Shimada, Y. Hatano, P. Calderoni, T. Oda, Y. Oya, M. Sokolov, K. Zhang, G. Cao, R. Kolasinski, and J. P. Sharpe, First result of deuterium retention in neutron-irradiated tungsten exposed to high flux plasma in TPE, *J. Nucl. Mater.* **415**, S667 (2011).
- [53] O. V. Ogorodnikova, Fundamental aspects of deuterium retention in tungsten at high flux plasma exposure, *J. Appl. Phys.* **118**, 074902 (2015).
- [54] R. Kirchheim, Solid solutions of hydrogen in complex materials, in *Solid State Physics* Vol. 59, edited by H. Ehrenreich and F. Spaepen, (Elsevier, Amsterdam, 2004), pp. 203.
- [55] E. Hayward, R. Hayward, and C.-C. Fu, Predicting distinct regimes of hydrogen behavior at nano-cavities in metals, *J. Nucl. Mater.* **476**, 36 (2016).
- [56] A. Chartier, C. Onofri, L. Van Brutzel, C. Sabathier, O. Dorosh, and J. Jagielski, Early stages of irradiation induced dislocations in uranium, *Appl. Phys. Lett.* **109**, 181902 (2016).
- [57] J. Byggmästar, F. Granberg, A. E. Sand, A. Pirttikoski, R. Alexander, M. C. Marinica, and K. Nordlund, Collision cascades overlapping with self-interstitial defect clusters in Fe and W, *J. Phys.: Condens. Matter* **31**, 245402 (2019).
- [58] A. Fellman, A. E. Sand, J. Byggmästar, and K. Nordlund, Radiation damage in tungsten from cascade overlap with voids and vacancy clusters, *J. Phys.: Condens. Matter* **31**, 405402 (2019).
- [59] F. Granberg, K. Nordlund, M. W. Ullah, K. Jin, C. Lu, H. Bei, L. M. Wang, F. Djurabekova, W. J. Weber, and Y. Zhang, Mechanism of Radiation Damage Reduction in Equiatomic Multicomponent Single Phase Alloys, *Phys. Rev. Lett.* **116**, 135504 (2016).
- [60] J. Byggmästar, F. Granberg, and K. Nordlund, Effects of the short-range repulsive potential on cascade damage in iron, *J. Nucl. Mater.* **508**, 530 (2018).
- [61] G. Veliša, M. W. Ullah, H. Xue, K. Jin, M. L. Crespillo, H. Bei, W. J. Weber, and Y. Zhang, Irradiation-induced damage evolution in concentrated Ni-based alloys, *Acta Mater.* **135**, 54 (2017).
- [62] F. Granberg, J. Byggmästar, and K. Nordlund, Molecular dynamics simulations of high-dose damage production and defect evolution in tungsten, *J. Nucl. Mater.* **556**, 153158 (2021).
- [63] S. Zhang, K. Nordlund, F. Djurabekova, F. Granberg, Y. Zhang, and T. S. Wang, Radiation damage buildup by athermal defect reactions in nickel and concentrated nickel alloys, *Mater. Res. Lett.* **5**, 433 (2017).
- [64] D. R. Mason, D. Nguyen-Manh, and C. S. Becquart, An empirical potential for simulating vacancy clusters in tungsten, *J. Phys.: Condens. Matter* **29**, 505501 (2017).
- [65] S. Plimpton, Fast parallel algorithms for short-range molecular dynamics, *J. Comput. Phys.* **117**, 1 (1995).
- [66] M. Ghaly, K. Nordlund, and R. S. Averback, Molecular dynamics investigations of surface damage produced by kilo-electronvolt self-bombardment of solids, *Philos. Mag. A* **79**, 795 (1999).

- [67] K. Nordlund, M. Ghaly, R. S. Averback, M. Caturla, T. Diaz de la Rubia, and J. Tarus, Defect production in collision cascades in elemental semiconductors and FCC metals, *Phys. Rev. B* **57**, 7556 (1998).
- [68] K. Nordlund, Molecular dynamics simulation of ion ranges in the 1-100 keV energy range, *Comput. Mater. Sci.* **3**, 448 (1995).
- [69] A. E. Sand, S. L. Dudarev, and K. Nordlund, High-energy collision cascades in tungsten: Dislocation loops structure and clustering scaling laws, *Europhys. Lett.* **103**, 46003 (2013).
- [70] H. J. C. Berendsen, J. P. M. Postma, W. F. van Gunsteren, A. DiNola, and J. R. Haak, Molecular dynamics with coupling to external bath, *J. Chem. Phys.* **81**, 3684 (1984).
- [71] R. S. Averback and K. L. Merkle, Radiation-annealing effects in energetic displacement cascades, *Phys. Rev. B* **16**, 3860 (1977).
- [72] J. D. Honeycutt and H. C. Andersen, Molecular dynamics study of melting and freezing of small Lennard-Jones clusters, *J. Phys. Chem.* **91**, 4950 (1987).
- [73] A. Stukowski, Structure identification methods for atomistic simulations of crystalline materials, *Modell. Simul. Mater. Sci. Eng.* **20**, 045021 (2012).
- [74] A. Stukowski, Visualization and analysis of atomistic simulation data with OVITO—the open visualization tool, *Modell. Simul. Mater. Sci. Eng.* **18**, 015012 (2009).
- [75] R. Bullough, The cracked dislocation under tension, *Philos. Mag.* **9**, 917 (1964).
- [76] PLANSEE Metall GmbH High Performance Materials, PLANSEE, A-6600 Reutte, Austria, <http://www.plansee.com>.
- [77] A. Manhard, M. Balden, and S. Elgeti, Quantitative microstructure and defect density analysis of polycrystalline tungsten reference samples after different heat treatments, *Practical Metallography* **52**, 437 (2015).
- [78] T. Schwarz-Selinger, Deuterium retention in MeV self-implanted tungsten: Influence of damaging dose rate, *Nucl. Mater. Energy* **12**, 683 (2017).
- [79] J. F. Ziegler, J. P. Biersack, and U. Littmark, *The Stopping and Range of Ions in Solids* (Pergamon, Oxford, 1982).
- [80] R. E. Stoller, M. B. Toloczko, G. S. Was, A. G. Certain, S. Dwaraknath, and F. A. Garner, On the use of SRIM for computing radiation damage exposure, *Nucl. Instrum. Methods Phys. Res., Sect. B* **310**, 75 (2013).
- [81] ASTM E521-16, *Standard Practice for Investigating the Effects of Neutron Radiation Damage Using Charged-Particle Irradiation*, Standard (ASTM International, West Conshohocken, PA, 2016).
- [82] S. Kapsner, M. Balden, T. F. da Silva, S. Elgeti, A. Manhard, K. Schmid, T. Schwarz-Selinger, and U. von Toussaint, Influence of sub-surface damage evolution on low-energy-plasma-driven deuterium permeation through tungsten, *Nucl. Fusion* **58**, 056027 (2018).
- [83] A. Manhard, T. Schwarz-Selinger, and W. Jacob, Quantification of the deuterium ion fluxes from a plasma source, *Plasma Sources Sci. Technol.* **20**, 015010 (2011).
- [84] M. Pecovnik, T. Schwarz-Selinger, and S. Markelj, Experiments and modelling of multiple sequential MeV ion irradiations and deuterium exposures in tungsten, *J. Nucl. Mater.* **550**, 152947 (2021).
- [85] E. A. Hodille, Y. Ferro, N. Fernandez, C. S. Becquart, T. Angot, J. M. Layet, R. Bisson, and C. Grisolia, Study of hydrogen isotopes behavior in tungsten by a multi trapping macroscopic rate equation model, *Phys. Scr.*, **T167**, 014011 (2016).
- [86] M. Pečovnik, E. A. Hodille, T. Schwarz-Selinger, C. Grisolia, and S. Markelj, New rate equation model to describe the stabilization of displacement damage by hydrogen atoms during ion irradiation in tungsten, *Nucl. Fusion* **60**, 036024 (2020).
- [87] M. Zibrov, The Influence of Radiation, Mechanical, and Plasma-Induced Damage on Deuterium Retention in Tungsten, Ph.D. thesis, Technical University of Munich (2019).
- [88] E. Hayward and C.-C. Fu, Interplay between hydrogen and vacancies in α -Fe, *Phys. Rev. B* **87**, 174103 (2013).
- [89] K. Sugiyama, K. Schmid, and W. Jacob, Sputtering of iron, chromium and tungsten by energetic deuterium ion bombardment, *Nucl. Mater. Energy* **8**, 1 (2016).
- [90] U. von Toussaint, A. Mutzke, K. Sugiyama, and T. Schwarz-Selinger, Simulation of coupled sputter-diffusion effects, *Phys. Scr.*, **T167**, 014023 (2016).
- [91] M. Shimada, G. Cao, Y. Hatano, T. Oda, Y. Oya, M. Hara, and P. Calderoni, The deuterium depth profile in neutron-irradiated tungsten exposed to plasma, *Phys. Scr.*, **T145**, 014051 (2011).
- [92] The subscript $_{\min}$ reminds us to use the minimum image convention when adding or subtracting vectors in a periodic supercell. Henceforth we will drop this subscript for clarity of notation.
- [93] M. P. Allen and D. J. Tildesley, *Computer Simulation of Liquids* (Clarendon, Oxford, 1987).